MINISTRY OF EDUCATION
AND TRAINING

VIETNAM ACADEMY OF SCIENCE
AND TECHNOLOGY

GRADUATE UNIVERSITY OF SCIENCE AND TECHNOLOGY

Tran Thi Thai

THE SOURCES OF COSMIC RE-IONIZATION AS SEEN BY MUSE/VLT

SUMMARY OF DISSERTATION ON SCIENCES OF MATTER

Major: Atomic and Nuclear Physics

Code: 9 44 01 06

Hanoi - 2024

The dissertation is completed at: Graduate University of Science and Technology, Vietnam Academy Science and Technology

Supervisors:

1. Supervisor 1: Dr. Pham Tuan-Anh, Vietnam National Space Center
2. Supervisor 2: Dr. Roser Pello, Aix-Marseille University, France

Referee 1: Associate Professor Ngo Ngoc Hoa, Hanoi National University of Education

Referee 2: Professor Dao Tien Khoa, Vietnam Atomic Energy Commission

Referee 3: Associate Professor Do Quoc Tuan, Phenikaa University

The dissertation is examined by Examination Board of Graduate University of Science and Technology, Vietnam Academy of Science and Technology at 9am on August 29th, 2024

The dissertation can be found at:

1. Graduate University of Science and Technology Library
2. National Library of Vietnam

1 Introduction

The success in operating astronomical instruments in recent years, such as Multi-Unit Spectroscopic Explorer (MUSE) at the Very Large Telescope (VLT), James Webb Space Telescope (JWST), etc., has driven research in the early Universe to become more dynamic than ever before. The ultimate goal of scientists working in this field is to study the sources of cosmic re-ionization and estimate their contribution to the re-ionization budget.

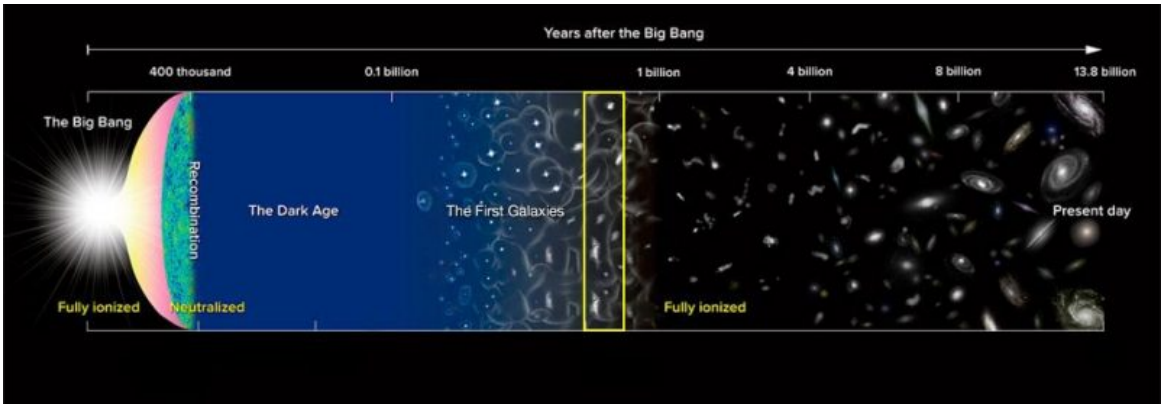

Figure 1.1: A brief history of the Universe from the Big Bang. The horizontal axis traces back time (top). The evolution phases of the Universe are shown from the time when the matter was fully ionized right after the Big Bang; after 380'000 years the recombination happened, at a redshift of 1100; after a few hundred million years the formation of the first structures (first stars, and galaxies) at the redshift of ~ 10, marked the end of the Dark Ages; the re-ionization was completed at redshift ~ 6. Credit: NAOJ

After the Big Bang, the temperature of the Universe was so hot that protons and electrons could not combine together to form the neutral hydrogen atoms. As the Universe expanded, its temperature cooled down, at $\sim$ 3000K, it was cool enough for the formation of neutral hydrogen, marking the beginning of the Dark Ages. The Universe became transparent and the radiation from the Big Bang referred to as Cosmic Microwave Background could freely travel. Over time, the Universe continued to expand and cool creating conditions for the formation of the first structures such as stars and galaxies. The radiation from these structures will ionize the neutral hydrogen atoms surrounding them, marking the end of the Dark Ages and the beginning of the Epoch of re-ionization. This is considered a crucial stage in the evolution of the Universe.

Up to now, our understanding of the sources responsible for the reionization process remains unclear. It could be active galactic nuclei (AGN) with notable characteristics such as high brightness and high escape fraction of ionizing photons. However, the number of AGNs at redshift $z \geq 6$ that have been identified at the moment is not enough to maintain the epoch of re-ionization. Alternatively, it could be star-forming galaxies that provide ionizing photons thanks to young and massive stars. To address the stated question, the best

approach is to study the contribution of these sources to the reionization process. In this thesis, I investigate the contribution of star-forming galaxies by studying the evolution of the Lyman-alpha Luminosity Function with redshift, providing valuable information regarding the galaxy density distribution within a given redshift range. Previous studies have predicted that faint, low-mass star forming galaxies significantly contribute to the reionization process. To strengthen these predictions, quantitative calculations and a more comprehensive picture need to be developed. However, current observations in the field have not yet reached the faintest limit of luminosity, while observations based on gravitational lensing phenomena show improvement due to magnification. This thesis condenses on the galaxies emitting the Lyman alpha behind lensing clusters observed by MUSE/VLT.

This chapter introduces the research topic, the current understanding of the first structures in the Universe, the ionization and recombination process. It also provides an overview of the spectral properties of star-forming galaxies, including characteristic features and methods to identify them from a given data cube. As we know, hydrogen is the most abundant element in the Universe, and electrons in the outer shell are easily excited to higher energy states in the interstellar medium so, Lyman alpha is the strongest line observable by ground-based optical astronomical telescopes. To date, there are a number of galaxies have already detected at redshift $z \geq 6$, $\sim$ 10000 galaxies at redshift $z \geq 4$ from HST observations ([1, 2]), $\sim$ 18000 galaxies spectroscopically identified with Lyman alpha emission (HETDEX) at a redshift range of $z \simeq 2.0-3.5$ ([3]). The abundance of identified galaxies raises a question about their density in the early Universe and their contribution to the cosmic reionization. This leads us to the definition of the Luminosity Function which tells us about number of galaxies that can be detected in a given luminosity range and a given cosmic co-moving volume. Studying the evolution of the Lyman alpha emitters luminosity function as a function of redshift is the most active branch at present to address the stated issue.

In Chapter 1, I also present an overview of recent results using observational Lyman alpha line data from astronomical observatories, combined with various approaches to probe the evolution of the Luminosity Function with redshift. However, information about the faint sources is limited as observations have not yet reached the necessary depth. The assumption of the slope value (α=$-1.5, -2.0, -2.5$) for the Schechter function is often applied to recent research ([4, 5]) during fitting the Luminosity function points. Scientific progress requires observational data to confirm theoretical models and estimate the galaxy density more accurately. Therefore, the thesis raises the issue of observing star-forming galaxies based on the gravitational lensing effect, a consequence of the relativistic Einstein theory, to obtain signals of faint Lyman alpha emitters.

2 The MUSE Lensing Project: from observations of massive clusters to LAE sample selection

This chapter briefly presents information about the Multi-Unit Spectroscopic Explorer (MUSE/VLT), its scientific goals, and the recent impressive results. The spectrograph provides a spectrum for every pixel in a MUSE Field of View. The collected data contains information about the spatial location of the object, and its spectra in different wavelengths covering a range of 4750 Å to 9370 Å corresponding to the redshift of Lyman Alpha Emitters at a redshift range $2.9 \leq z \leq 6.7$.

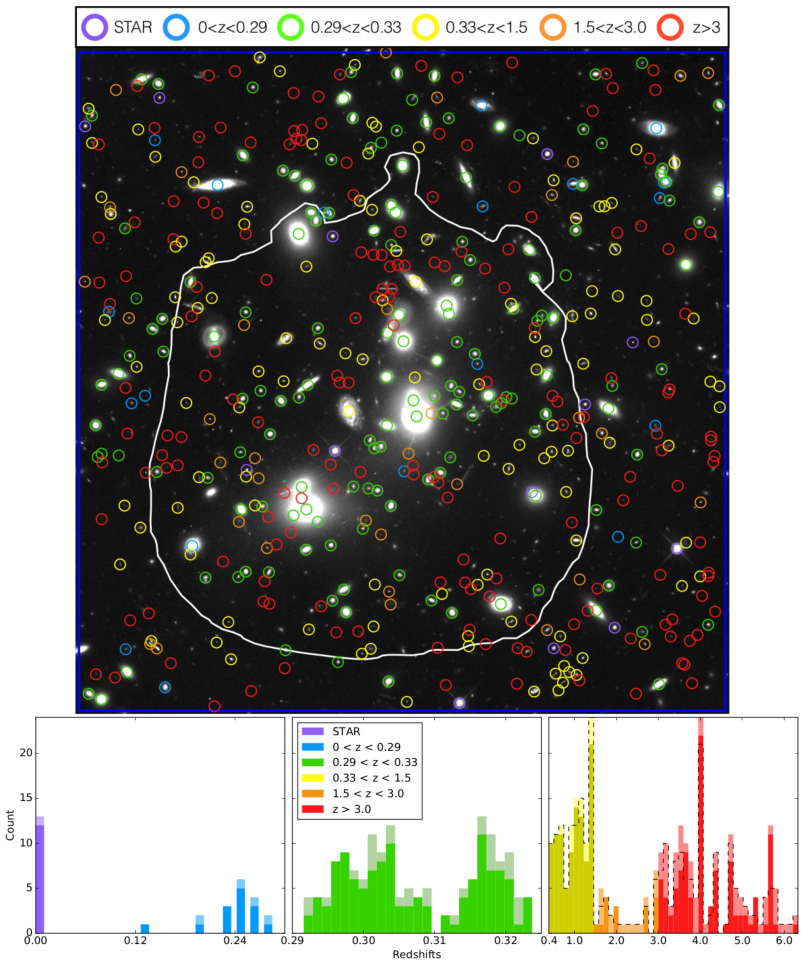

Figure 2.1: Upper panel: Spatial distribution of sources behind gravitational lensing cluster A2744 observed by MUSE and RGB HST. Lower panel: Redshift distribution of the sources. Credit: [6]

In the third part of the chapter, I present the general features of 17 lensing clusters based on previous results and mass models of these clusters. Figure 2.1 is an example of spatial source distribution observed by MUSE in the Field of A2744. The different color circles denote the redshift of the sources. Figure 2.2 illustrates the procedure of inspection of the Lyman alpha emitter behind A2667 and determining its redshift value. To avoid

subjective opinions during source inspection, there are three independent expert groups involved, followed by a joint meeting to reach the final conclusion about the redshift of the source and its confidence level. There are three different levels to assess the reliability of the redshift value of a source:

- $zconf$=1: is the lowest level. At this level, the redshift of a source is identified based on a single weak emission line. We did not have 100% confidence to say that it is a Lyman alpha line, so this source was not used to study the Luminosity function of Lyman alpha emitters in the thesis. However, we discussed the effect of these sources on the uncertainty slope values of the Schechter function at different redshift ranges assuming they were included in the final data sample.

- $zconf$=2. At this level, the redshift value of a source is identified based on several emission lines. In some cases when the lines are not strong enough, but the observed image belongs to multiple systems, the confidence level of the redshift will be upgraded from $zconf$=1 to $zconf$=2.

- $zconf$=3: the highest confidence level. The redshift of the source is measured based on several strong emission lines combined with absorption lines, the line profile that shows identified features.

Because of the lensing effect, the signal from distant galaxies has been magnified, and the images have been distorted allowing the observation of multiple images of the same system. It is a complex analysis due to the requirement of projection back and forth between the source and image plane. Aiming to limit computational redundancy and save time, in the context of my thesis, I selected only one representative image for each system based on criteria such as high SNR, reasonable magnification value, and the most isolated image compared to the others. The Chapter 2 concluded with general information about 600 Lyman alpha emitters behind 17 lensing clusters with redshift in the range $2.9 \leq z \leq 6.7$ (Table 2.1) covering four luminosity ranges $39 \leq \log L[\mathrm{erg/s}] \leq 43$ and compared with data from a previous study conducted by [7].

There are two things worth mentioning when computing the Lyman alpha Emitters Luminosity Function:

- Flux of the sources. The data obtained from MUSE is stored as a data cube (2 spatial dimensions and 1 spectral dimension) so flux is measured by spectral fitting method using a function proposed by [8]:

$$f(\lambda) = A \exp \frac{-(\lambda - \lambda_0)^2}{2(a(\lambda - \lambda_0) + d)^2} \tag{2.1}$$

where, A is the amplitude of the Lyman alpha spectra, a is asymmetric value of the Lyman alpha profile, d is FWHM. These parameters are optimized during fitting by applying the function form above to a subcube with a size of 5" $\times$ 5" $\times$ 12.5Å surrounding the source position. The mean value of FWHM and asymmetry were found to be 7Å and 0.2, respectively. The total flux value of the sources is taken from [9]. In the case of faint sources in which the profile could not fit with the above equation, we use values obtained from the Source Extractor software which did not assume a parametric profile for the line. A comparison of flux values obtained from the two methods is presented in Figure 2.3 (left). The abscissa axis

displays flux values measured from the Source Extractor and the vertical axis is from spectral fitting, both in the unit of 10^{-18} [erg/s]. Linear fitting with a coefficient of 0.9 indicates the similarity between the two methods.

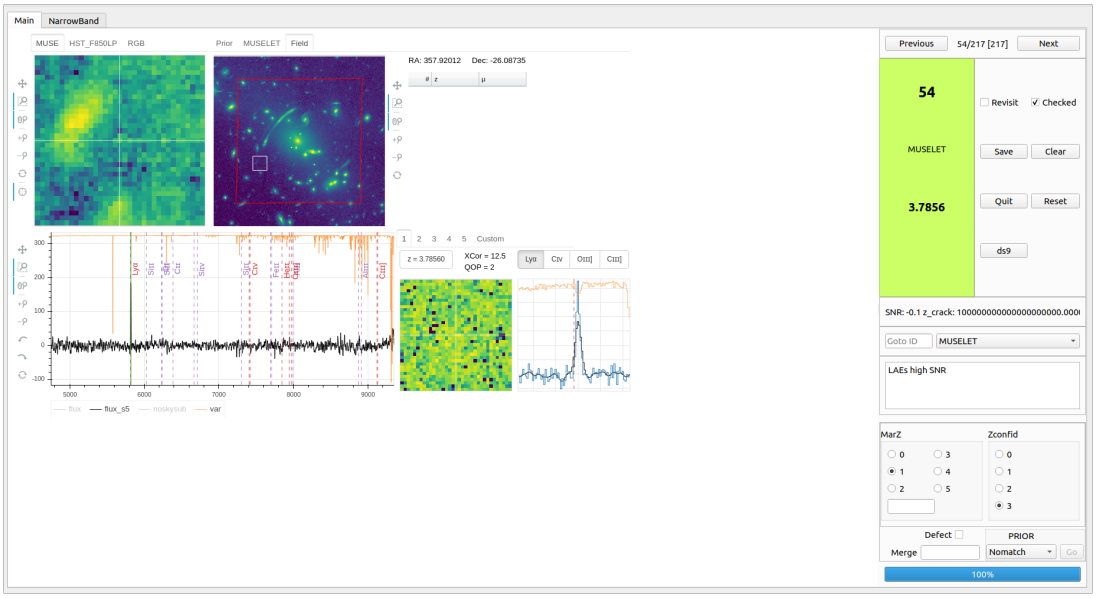

Figure 2.2: Interface of the source inspector software used to identified M54 source behind lensing cluster A2667 observed by MUSE and HST. The M54 is not well identified by HST observation (upper panel on the left). The upper panel on the right is A2667 MUSE FoV, the small red square denotes the region in which M54 is identified. Its spectra and zoomed-in profile are shown in the lower panel. The confidence level has been determined and recorded in the right column.

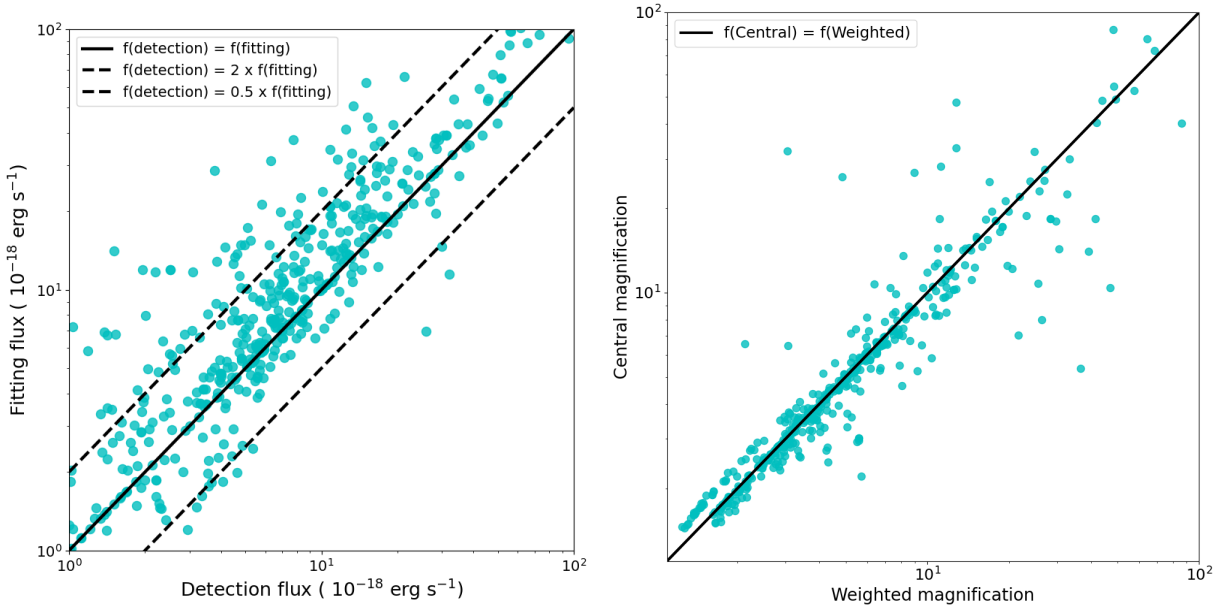

Figure 2.3: Left: Fluxes comparison obtained from two methods: Spectral fitting (y-axis) and Source Extractor (x-axis). Right: Magnification comparison at central source (y-axis) and its weighted value (x-axis).

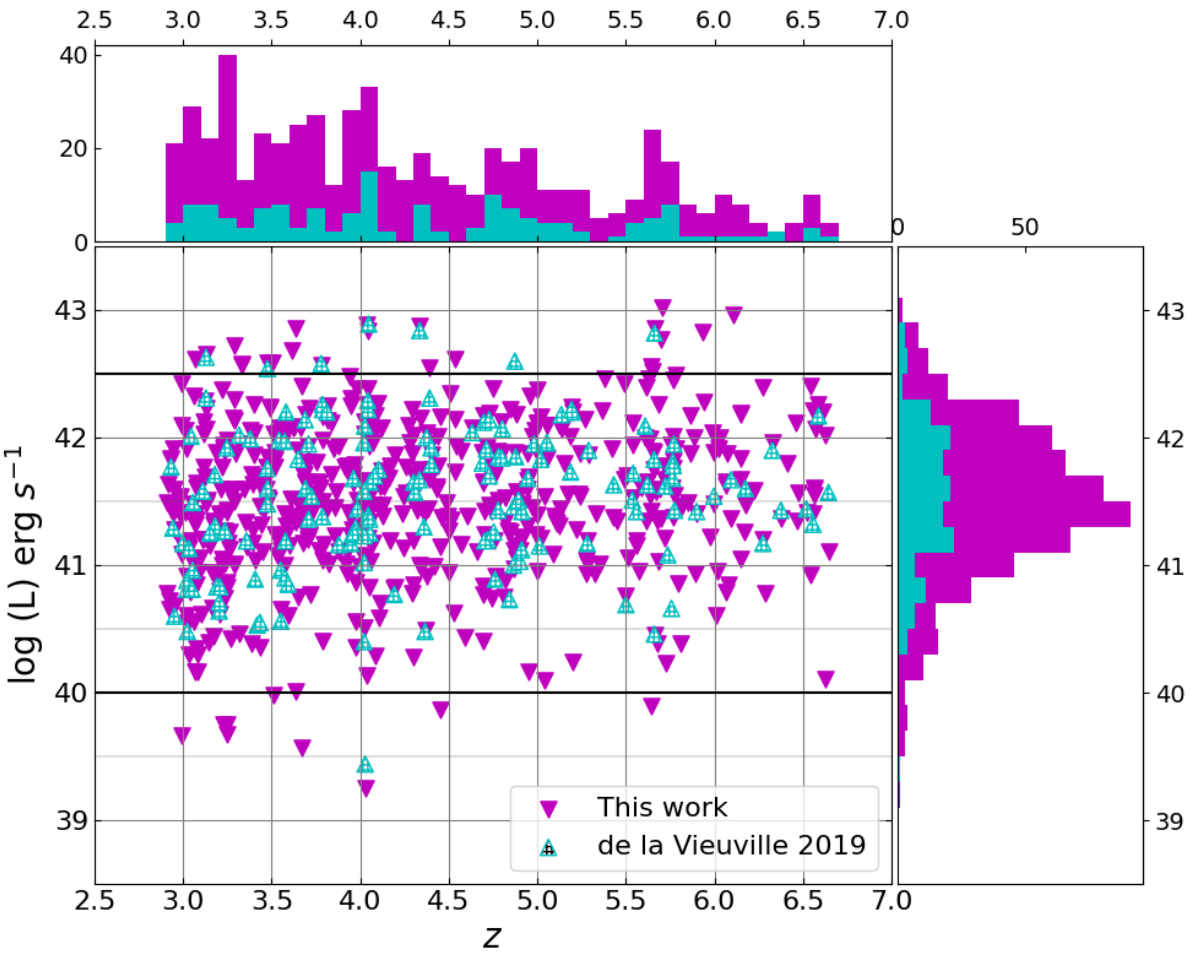

Figure 2.4: Central panel: Luminosity versus the redshift of the source. Top panel: Redshift distribution. Right panel: Luminosity distribution. The magenta color denotes values of 600 Lyman alpha Emitters used in the thesis compared to the data from [7] in cyan.

- Magnification value. [9] computed the magnification value of the source at its central position. In the case of an extended Lyman alpha image, the magnification varies across the image and the magnification value at one point of the image may not reflect the average magnification value of the Lyman alpha emission in the image. To better account for extended sources, we prefer to use the weight value that has already accounted for this effect. The difference between these two values is illustrated in Figure 2.3 (right).

Compared to the previous data by [7] probing Lyman alpha emitters behind four lensing clusters, the number of sources in the current study is four times more. At the faintest level $\log L[\mathrm{ergs}^{-1}] \sim 40$, it indicates a significantly larger number of the sources in this work compared to the previous one. Therefore, the data used in the present work substantially improves the statistical data sample in this range. Figure 2.4 compares the current data with the previous data used in [7].

Table 2.1

General information of 17 lensing clusters observed by MUSE

Cluster	RA	DEC	z	Programme ID	Notes	Seeing value	MUSE depth (hrs)	N. LAEs
A2390	21:53:36.823	+17:41:43.59	0.228	094.A-0115		0.75	2	7
A2667	23:52:28.400	-26:05:08.00	0.233	094.A-0115		0.62	2	14
A2744	00:14:20.702	-30:24:00.63	0.308	094.A-0115, 095.A-0181	MACS, FF	0.61	3.5-7	128
A370	02:29:53.122	-01:34:56.14	0.375	094.A-0115, 096.A-0710	FF	0.66	1.5-8.5	41
AS1063	22:48:43.975	-44:31:51.16	0.348	60.A-9345, 095.A-0653	FF	1.02	3.9	20
BULLET	06:58:38.126	-55:57:25.87	0.296	094.A-0115		0.56	2	11
MACS0257	02:57:41.070	-22:09:17.70	0.322	099.A-0292, 0100.A-0249	MACS	0.52	8	24
MACS0329	03:29:41.568	-02:11:46.41	0.450	096.A-0105	MACS, CLASH	0.69	2.5	16
MACS0416N	04:16:09.144	-24:04:02.95	0.397	094.A-0115, 0100.A-0763	MACS, CLASH	0.53	17	45
MACS0416S	04:16:09.144	-24:04:02.95	0.397	094.A-0525	MACS, CLASH	0.65	11-15	32
MACS0451	04:51:54.647	+00:06:18.21	0.430	098.A-0502, 0104.A-0489	MACS	0.58	8	21
MACS0520	05:20:42.046	-13:28:47.58	0.336	098.A-0502, 0104.A-0489	MACS	0.57	8	19
MACS0940	09:40:53.698	+07:44:25.31	0.335	098.A-0502, 0101.A-0506	MACS	0.571	8	48
MACS1206	12:06:12.149	-08:48:03.37	0.438	095.A-0181, 097.A-0269	MACS, CLASH	0.521	4-9	49
MACS2214	22:14:57.292	-14:00:12.91	0.502	099.A-0292, 0101.A-0506	MACS	0.55	7	17
RXJ1347	13:47:30.617	-11:45:09.51	0.451	095.A-0525, 097.A-0909	MACS, CLASH	0.551	2-3	72
SMACS2031	20:31:53.256	-40:37:30.79	0.331	60.A-9100	MACS	0.79	10	20
SMACS2131	21:31:04.831	-40:19:20.92	0.442	0101.A-0506, 0102.A-0135	MACS	0.59	7	16
			Total:				**107-128**	**600**

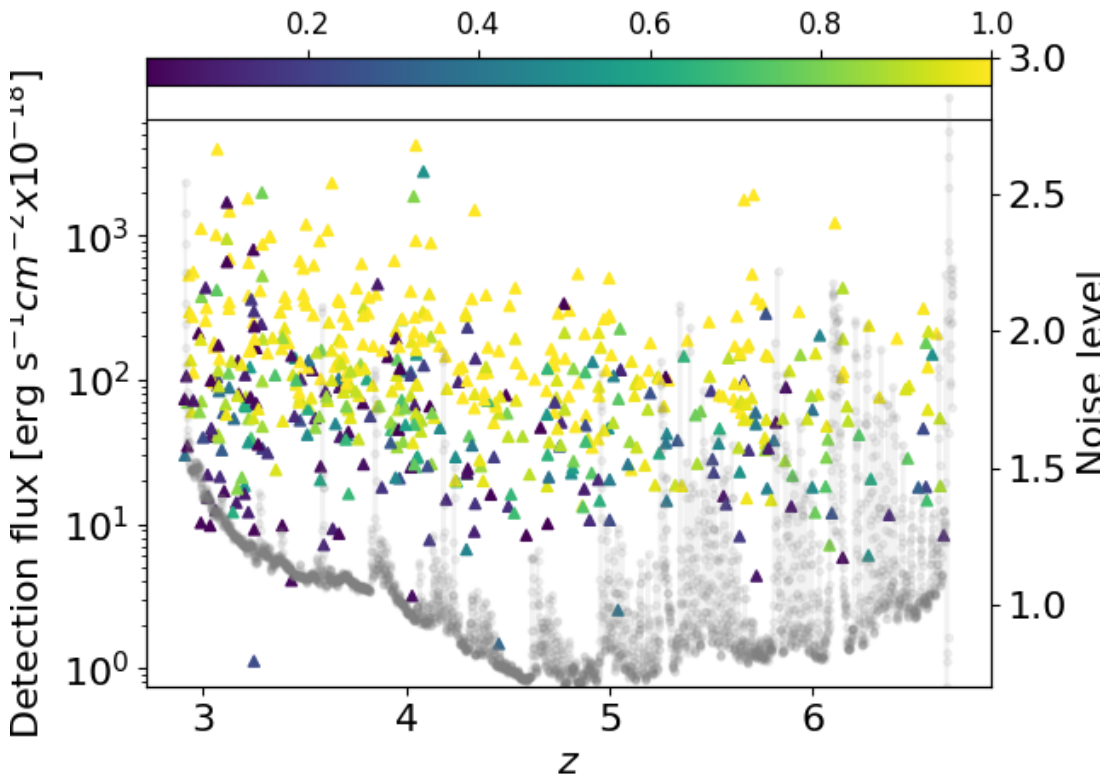

Figure 2.5: Detection flux and noise level in the sample versus redshift. The left axis displays the detected flux, the right axis gives the noise level (normalized), the lower horizontal axis is redshift and the upper one shows the completeness scale. The gray circles represent the evolution of noise level with redshift from the observation through the spectral dimension of the MUSE cube.

3 Computing the Luminosity Function in Lensing Clusters

Chapter 3 describes the process of computing the $V_{\max}$ value for each source within our survey. In another way, $V_{\max}$ is the volume of a survey in which individual sources could be detected ([10]). The contribution of the source to the density of galaxies is given by the reciprocal of this parameter. This thesis includes data collected in 18 fields (MACS0416 was observed in two fields); therefore, the $V_{\max}$ of individual sources must be calculated for all regions of the survey, including those where the source is absent. Working in the image plane to compute $V_{\max}$ value of individual sources may lead to an overestimate of this value.

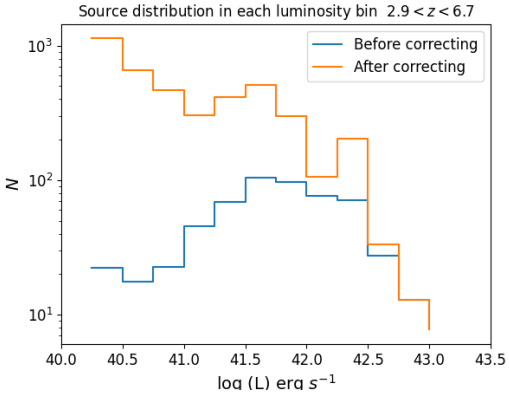

Figure 3.1: Source distribution in the redshift interval $2.9 \leq z \leq 6.7$ for a luminosity bin width of 0.25 in logarithmic scale. The blue and orange lines are the distribution before and after correcting for completeness.

For this reason, the present work has been done in the source plane, based on the creation of 3D cube in the source plane for each source. The pipeline was initially developed by [7] to study the Luminosity Function of 128 Lyman alpha emitters behind only four lensing clusters. In this chapter, I summarize the main steps, with some new improvements that have been taken into account for the calculation procedure, and make a comparison of the obtained result on the volume of the survey to the previous work. It is worth mentioning that the present results indicate a total co-moving volume of approximately 50000 Mpc^3, which is three times larger than that in [7]. However, this value is significantly smaller than the one found in the works using data observed in the blank fields, due to the constraints imposed by gravitational lensing effects.

Cluster	Total co-moving volume [Mpc^3]
A2390	735
A2667	885
A2744	10500
A370	5350
AS1063	1970
BULLET	895
MACS0257	730
MACS0329	1225
MAC0416N	3420
MACS0416S	1670
MACS0451	1210
MACS0520	765
MACS0940	5760
MACS1206	2980
MACS2214	1100
RXJ1347	7920
SMACS2031	1675
SMACS2131	920
Total	49710

Table 3.1: Total co-moving volume of 17 gravitational lensing clusters in the present work within a redshift range of $2.9 \leq z \leq 6.7$.

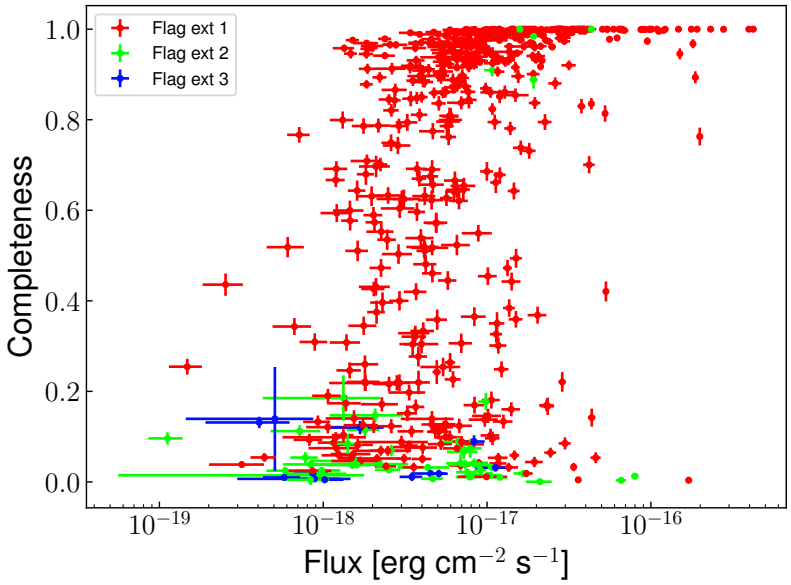

Figure 3.2: Completeness vs. detection flux of LAEs from the present sample. Different colors indicate the quality of extraction from Source Extractor.

4 Luminosity Function

Chapter 4 presents the main results of the thesis on the Luminosity Function of 600 Lyman alpha emitters in four redshift intervals. By definition, the Luminosity Function is the number of galaxies per unit of co-moving volume (number density), per luminosity interval. To compute the Luminosity Function, in addition to determining the $V_{\rm max}$ of a source as described above, one must account for the fact that not all sources in the data sample have a 100% probability of being detected. Hence, we need to correct for completeness, which gives the true probability of finding a source in the cube. The procedure was carried out for each source by reconstructing the profile of the galaxy in the image plane and randomly injecting this model into different places in the cube, to capture the real effect of the noise. The source is considered to be detected when the maximum deviation between the injected position and the detected position of the source is less than 0.8". The completeness is determined directly by the ratio between the number of successful detections, under the same conditions as the original extraction, and the number of objects injected. There are several differences between this work and that of [7] in consideration of completeness, as well as in the detailed discussion of selection effects.

- The impact of image size on the final result of completeness value has been discussed. The size has to be large enough to capture the noise in the source region of the slice where the Lyman alpha emission line reaches the peak. In the thesis, I increase the size from 30" $\times$ 30" to 80" $\times$ 80".

- With the goal of maximizing the number of sources used for the Luminosity Function computation and subsequent advancements, we have excluded sources with completeness values below 1%. Compared to the work by [7], this value was set at 10%. Using 1% completeness for source detected correction is normal as the recent study on Luminosity Function did not mention the threshold, they believed that the sources were real because it was confirmed by the lensing model.

- The detected flux, noise level, and completeness with respect to the redshift of individual sources are shown in Figure 2.5. The number of sources used for the Luminosity Function in the whole redshift interval, for different luminosity intervals, has been presented in Figure 3.1, before and after completeness correction. Figure 2.5 shows that most faint sources have an extremely low completeness value. However, when the correction of the completeness parameter is taken into account, the number of sources in the low luminosity bins increases significantly. On the other hand, for sources allocated in the bright parts, the probability of detection is already high, so whether we apply the completeness correction or not does not markedly change the source distribution. In the luminosity range of $42.25 \leq \log L$ [erg s^{-1}] ≤ 42.5 of Figure 3.1, the appearance of a spike can be explained by the existence of low completeness sources.

Table 4.1: The best-fit values of the Schechter function at different redshift intervals.

Redshift	$\Phi*$ [10^{-4}Mpc^{-3}]	log $L*$[erg s^{-1}]	α
$2.9 \leq z \leq 6.7$	$7.41^{2.70}_{-2.20}$	$42.85^{0.10}_{-0.10}$	$-2.06^{0.07}_{-0.05}$
$2.9 \leq z \leq 4.0$	$6.56^{3.20}_{-2.40}$	$42.87^{0.11}_{-0.1}$	$-2.00^{0.07}_{-0.07}$
$4.0 \leq z \leq 5.0$	$4.06^{2.70}_{-1.70}$	$42.97^{0.13}_{-0.11}$	$-1.97^{0.09}_{-0.08}$
$5.0 \leq z \leq 6.7$	$3.49^{2.11}_{-1.50}$	$43.09^{0.10}_{-0.08}$	$-2.28^{0.12}_{-0.12}$

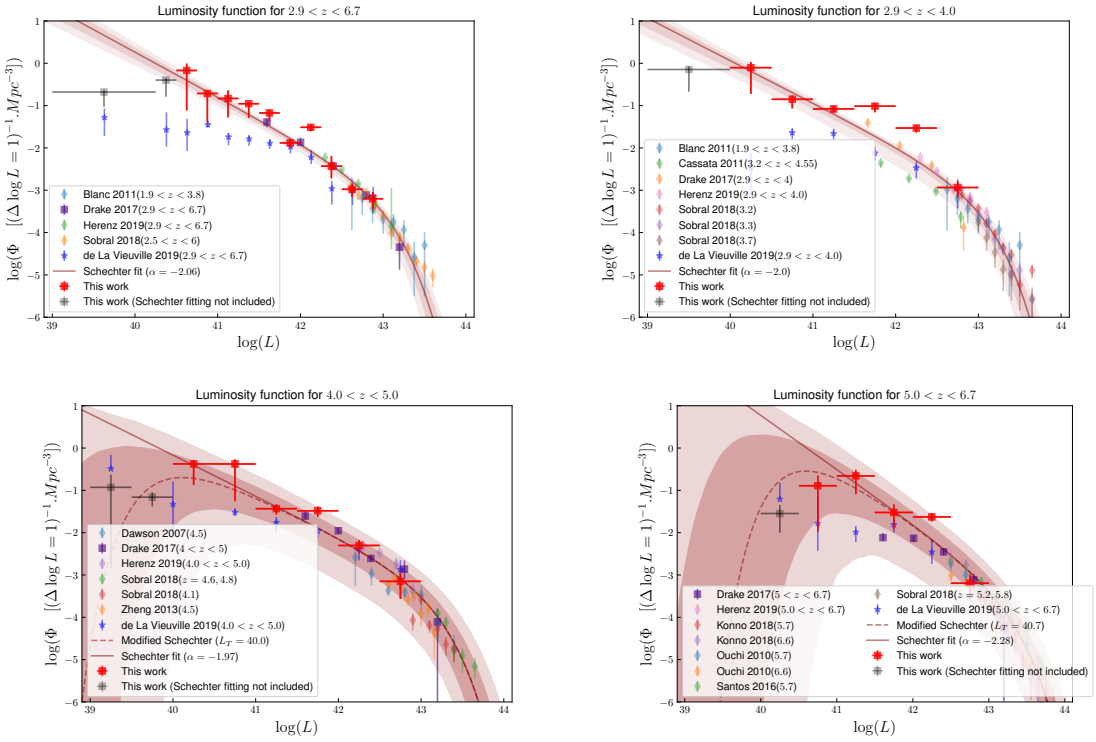

Figure 4.1: From left to right, top to bottom shows the Luminosity Function in different redshift intervals: $2.9 \leq z \leq 6.7$, $2.9 \leq z \leq 4.0$, $4.0 \leq z \leq 5.0$, and $5.0 \leq z \leq 6.7$. The red crosses represent the results of this work, while other colors in the bright end indicate data from the literature. The blue ones are results from [7] used for comparison. The solid brown reddish line is the best-fit Schechter function. The gray crosses obtained from the present work are not included in the fit. The reddish dashed lines correspond to the best fit with a modified Schechter function when taking into account the turnover in shape towards the faint luminosity regimes.

The Luminosity Function point within a given redshift bin and a given luminosity range follows the function below:

$$\Phi(L_i) \quad \frac{1}{\Delta \log L_i} \sum_j \frac{1}{C_j V_{\max,j}} \tag{4.1}$$

where $C_j, V_{\max,j}$ is the completeness and $V_{\max}$ of a given source, $\Delta \log L_i$ is the i^{th} luminosity bin width. The Luminosity Function points obtained from the present sample are fitted using

the Schechter function:

$$\Phi(L)dL \;\; \Phi* (\frac{L}{L*})^{\alpha} \exp(-\frac{L}{L*}) \frac{dL}{L*} \tag{4.2}$$

where α is the slope of the Schechter function at the faint end, $L*$ is the characteristic luminosity when the Schechter function transitions from exponential law at the bright end to the power law at the faint end, $\Phi*$ is the normalization factor. This luminosity function is investigated in four redshift intervals: $2.9 \leq z \leq 6.7$, $2.9 \leq z \leq 4.0$, $4.0 \leq z \leq 5.0$ and $5.0 \leq z \leq 6.7$. Using data collected from gravitational lensing clusters has proven to be effective in studying the Luminosity Function at the faint luminosity regime. However, such data becomes less effective at the nearby and higher characteristic luminosity values $L*$. This problem can be addressed by including the results from previous research on the Luminosity Function conducted within the same redshift and luminosity range as a constraint factor for the bright end of the Luminosity Function. The results of the Schechter function fitting are shown in Figure 4.1, with gray crosses excluded from the fit due to low completeness and highly magnified sources residing in these bins.

The best-fit values of the three free parameters of the Schechter function are presented in Table 4.1. The slope values α of the Schechter function display a slight evolution with redshift. Within the uncertainties, the $L*$ and $\Phi*$ are consistent with the previous results. The gray crosses in Figure 4.1 are not included during fitting, as most of the sources in these luminosity bins have high magnifications and small completeness values. Figure 4.2 displays the correlation of three free parameters in the Schechter function during fitting with a 68% confidence level. The LF points in each luminosity bin and each redshift interval are presented in Table 4.2.

At higher redshift intervals and fainter luminosity limits, several studies have discussed the possibility of a turnover in the shape of the Luminosity Function, such as [11, 12]. This is presented by gray crosses in Figure 4.1 that were not included during fitting. To gain a better understanding of this behavior, we have introduced a modified Schechter function by adding an exponential part to represent the observed configuration:

$$\Phi(L)\exp(-L_T/L)^m \;\; \frac{\Phi*}{L*}(\frac{L}{L*})^{\alpha} \exp(-L/L*)\exp((-L_T/L)^m) \tag{4.3}$$

where L_T is the value where the Luminosity Function starts showing a turnover, it is also the value in which $d\Phi/dL = 0$, m is the curvature value orienting the shape (upward if $m \leq 0$ or downward if $m>0$) of the faint part. This is presented in the lower panels of Figure 4.1. We found that m is about 1 while $\log L_T = 40$ and $\log L_T = 40.7$ [erg/s] with respect to the redshift range $4.0 \leq z \leq 5.0$ and $5.0 \leq z \leq 6.7$. Thanks to the lensing effect it allowed us to probe the evolution of the Luminosity Function with redshift at a fainter luminosity level compared to observations conducted in a blank field.

Table 4.2: Luminosity bins and Luminosity Function (LF) points with respect to different redshift intervals and different luminosity ranges

log (L) [erg/s]	log $(\phi)(\Delta(\log(L))\ 1)^{-1}$[Mpc^{-3}]	N	N_{corr}	$V_{\max}$ [Mpc^3]
$2.9 \leq z \leq 6.7$				
$39.00 \leq 39.63 \leq 40.25$	$-0.68^{0.04}_{-0.35}$	22.4	706.0	11827
$40.25 \leq 40.38 \leq 40.50$	$-0.40^{0.04}_{-0.39}$	17.6	645.4	15074
$40.50 \leq 40.63 \leq 40.75$	$-0.17^{0.16}_{-0.95}$	22.8	429.3	28457
$40.75 \leq 40.88 \leq 41.00$	$-0.71^{0.06}_{-0.68}$	45.2	301.5	31613
$41.00 \leq 41.13 \leq 41.25$	$-0.83^{0.19}_{-0.45}$	68.9	415.7	37344
$41.25 \leq 41.38 \leq 41.50$	$-0.96^{0.03}_{-0.33}$	105.0	547.9	41321
$41.50 \leq 41.63 \leq 41.75$	$-1.17^{0.07}_{-0.19}$	96.4	305.5	42227
$41.75 \leq 41.88 \leq 42.00$	$-1.88^{0.09}_{-0.11}$	76.4	105.1	46139
$42.00 \leq 42.13 \leq 42.25$	$-1.51^{0.07}_{-0.09}$	70.4	202.5	45795
$42.25 \leq 42.38 \leq 42.50$	$-2.43^{0.24}_{-0.29}$	27.5	33.5	47554
$42.50 \leq 42.63 \leq 42.75$	$-2.98^{0.13}_{-0.19}$	12.9	13.0	49295
$42.75 \leq 42.88 \leq 43.00$	$-3.20^{0.15}_{-0.25}$	7.7	7.8	49258
$2.9 \leq z \leq 4.0$				
$39.00 \leq 39.63 \leq 40.00$	$-0.15^{0.07}_{-0.52}$	6.64	415.33	1712
$40.00 \leq 40.25 \leq 40.50$	$-0.10^{0.13}_{-0.62}$	14.19	920.22	6114
$40.50 \leq 40.75 \leq 41.00$	$-0.85^{0.09}_{-0.22}$	34.0	396.17	11397
$41.00 \leq 41.25 \leq 41.50$	$-1.08^{0.07}_{-0.10}$	83.7	473.6	14529
$41.50 \leq 41.75 \leq 42.00$	$-1.01^{0.08}_{-0.14}$	69.5	148.0	15914
$42.00 \leq 42.25 \leq 42.50$	$-1.53^{0.06}_{-0.11}$	35.6	101.55	16327
$42.50 \leq 42.75 \leq 43.00$	$-2.93^{0.15}_{-0.23}$	10.0	10.0	17320
$4.0 \leq z \leq 5.0$				
$39.00 \leq 39.25 \leq 39.50$	$-0.93^{0.30}_{-1.91}$	1.0	38.0	730
$39.50 \leq 40.00 \leq 40.0$	$-1.16^{0.11}_{-0.22}$	2.4	48.3	4904
$40.0 \leq 40.25 \leq 40.5$	$-0.38^{0.09}_{-0.50}$	7.4	311.4	3159
$40.5 \leq 40.75 \leq 41.00$	$-0.38^{0.11}_{-0.88}$	19.6	205.1	7662
$41.00 \leq 41.25 \leq 41.50$	$-1.43^{0.10}_{-0.14}$	51.4	161.2	11044
$41.50 \leq 41.75 \leq 42.00$	$-1.48^{0.1}_{-0.15}$	55.0	148.5	12164
$42.00 \leq 42.25 \leq 42.50$	$-2.30^{0.13}_{-0.18}$	30.0	32.2	13182
$42.50 \leq 42.75 \leq 43.00$	$-3.15^{0.20}_{-0.42}$	4.7	4.8	13433
$5.0 \leq z \leq 6.7$				
$40.00 \leq 40.25 \leq 40.50$	$-1.55^{0.20}_{-0.45}$	6.0	23.8	4725
$40.50 \leq 40.75 \leq 41.00$	$-0.89^{0.24}_{-1.08}$	14.3	116.5	11105
$41.00 \leq 41.25 \leq 41.50$	$-0.66^{0.15}_{-0.43}$	38.9	705.5	13545
$41.50 \leq 41.75 \leq 42.00$	$-1.52^{0.19}_{-0.39}$	48.2	122.9	16190
$42.00 \leq 42.25 \leq 42.50$	$-1.63^{0.09}_{-0.11}$	32.3	105.2	16705
$42.50 \leq 42.75 \leq 43.00$	$-3.19^{0.2}_{-0.37}$	5.9	5.9	18542

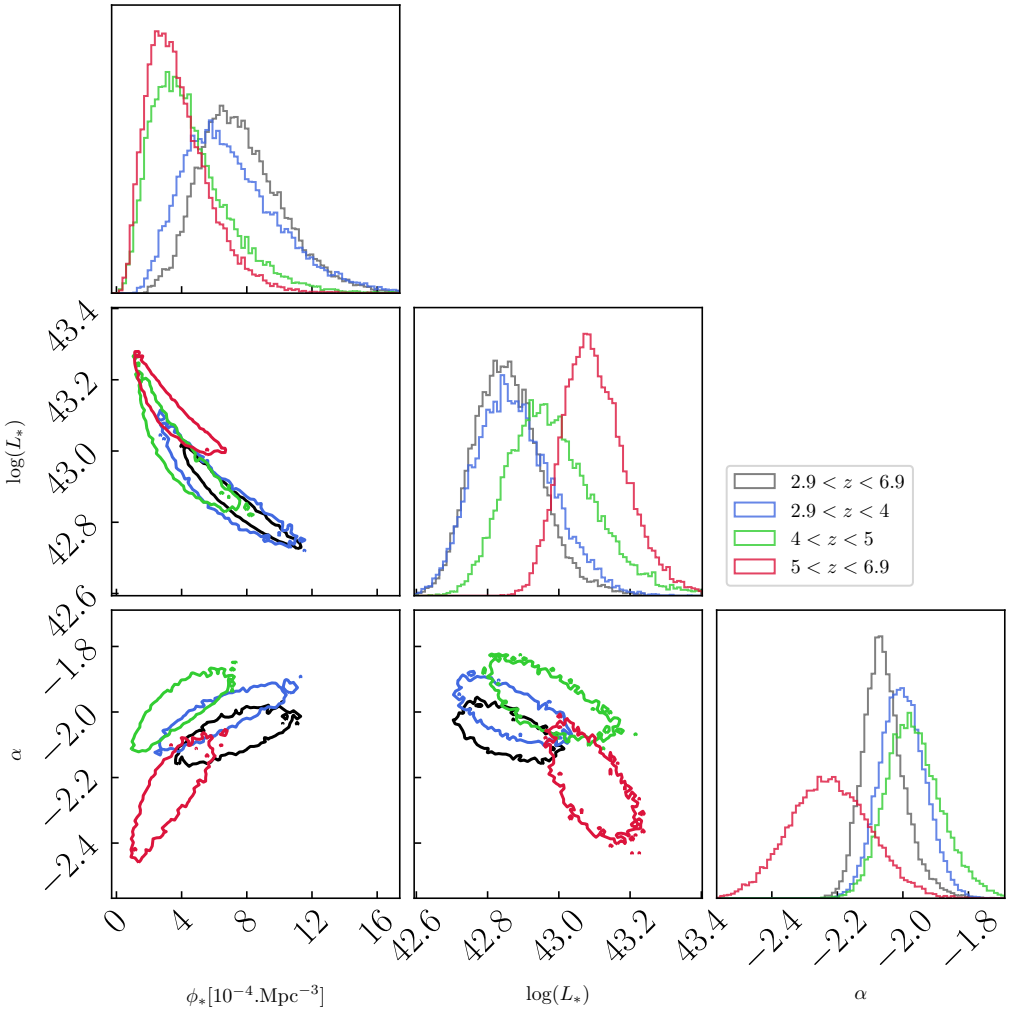

Figure 4.2: The correlation of three free parameters of the Schechter function with a 68% confident level.

Recently, two models have been developed by [13, 14] to predict the Lyman Alpha Emitters Luminosity Function at redshift $z \sim 6$. It is therefore necessary to compare the results of these models to those obtained in the present work for the highest redshift range $5.0 \leq z \leq 6.7$. The first model developed by [13] applies the SPHINX radiation hydrodynamics cosmological simulation to predict the Lyman Alpha Luminosity Function at the EoR by estimating the radiative transfer of the sources from ISM to the IGM scales. The second model, developed by [14] uses the AMIGA model to predict the possible scenarios of single and double ionization, taking into account the impact of galaxy formation and its evolution within their feedback on the IGM. The former predicts a single hydrogen ionization stage at redshift $z \sim 6$, while the latter predicts two reionization stages at redshift $z \sim 6$ and $z \sim 10$, with two separated phases defined by a short recombination episode. The results are shown in Figure 4.3. At the luminosity range $41 \leq \log L\,[\mathrm{erg/s}] \leq 42$, the prediction of AMIGA double reionization is in line with the one obtained from the SPHINX simulations after correction for the IGM. In general, the LF points are in good agreement with the two predictions without any normalization requirement. At the fainter luminosity, $\log L\,[\mathrm{erg/s}] \leq 41$, our LF points tend to depart from [14]. However, at this redshift interval, the uncertainty values are generally large, preventing us from evaluating the difference between the predictions. More observational

data at the faint end of the luminosity regime and high redshift ranges are needed to solve this problem.

In the thesis, we discuss the impacts of the criterion adopted by [7] to ignore sources that have completeness values below 10% and study the evolution of Luminosity Function with redshift. Finally, whether sources with completeness value below 1% or 10% are removed, the turnover in shape can still be seen in the vicinity of log L [erg/s] = 41.

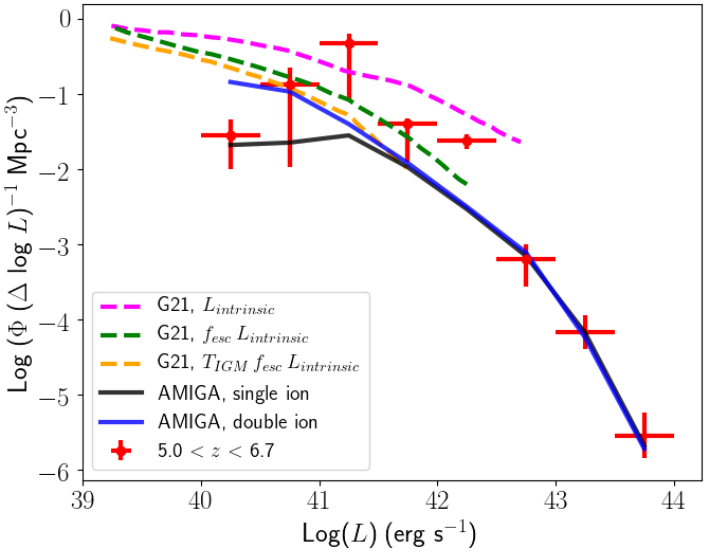

Figure 4.3: Comparision among the Luminosity Function points at the highest redshift interval $5.0 \leq z \leq 6.7$, the AMIGA model [14] and SPHINX simulations [13]. The pair of red crosses located in the brightest luminosity bins are average values from the literature. The blue and black solid lines are predicted from AMIGA models with respect to the single and double ionization scenarios [14]. The color dashed lines are predicted from SPHINX simulations [13] for the intrinsic luminosity value (magenta), correcting for the dust attenuation (blue) and IGM (orange).

The thesis also presents the effect of source selection on the shape of the Luminosity Function versus redshift. It is worth noting that, in the present work we are using sources with a high secure redshift ($zconf$ = 2, 3) to analyze the evolution of the Luminosity Function and ignore sources having a lower secure $zconf$ = 1 due to low signal to noise ratio or displaying an ambiguous line shapes. For this reason, we have conducted two tests by including half of $zconf$ = 1 and all the $zconf$ = 1 in the present data sample. The result showed that including $zconf$=1 in the final data sample did not significantly affect the shape of the Luminosity Function. In addition to source selection effects, we also discuss various factors contributing to systematic uncertainties in the faint end slope, including different completeness thresholds, different flux measurements, and varying fitting models. The final results are reported in Table 4.3.

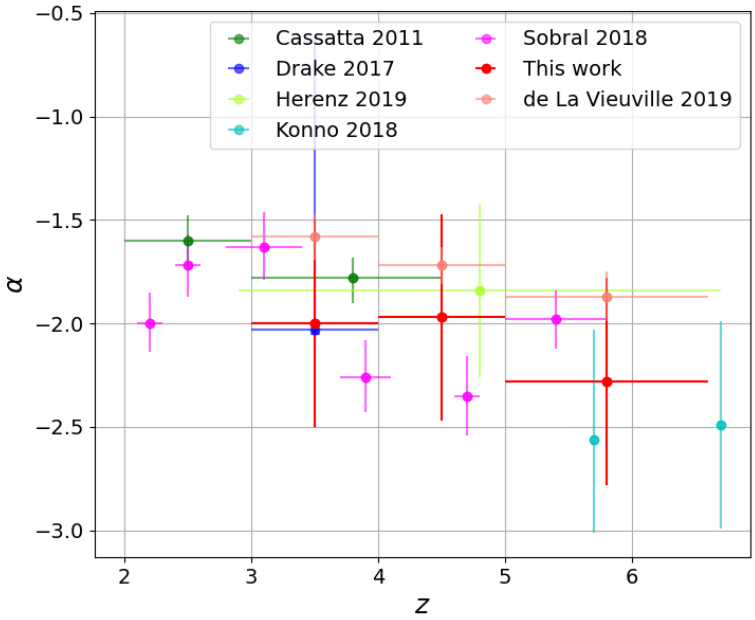

Figure 4.4: Evolution of the slope value with redshift. The error bars in the horizontal axis correspond to the redshift range of the survey.

Table 4.3: Faint-end slope values when applying different constraints

	z_{35}	z_{45}	z_{60}	z_{all}
Schechter fitting				
1% completeness	-2.00 ± 0.07	-1.97 ± 0.09	-2.28 ± 0.12	-2.06 ± 0.07
10% completeness	-1.78 ± 0.06	-1.83 ± 0.12	-1.75 ± 0.10	-1.46 ± 0.05
1% completeness and using the flux values obtained from Source Extractor	-2.10 ± 0.06	-1.97 ± 0.08	-2.24 ± 0.11	-1.82 ± 0.03
1% completeness and including all the $zconf = 1$ source	-1.83 ± 0.17	-1.92 ± 0.09	-1.94 ± 0.10	-2.29 ± 0.09
Linear fit				
1% completeness	-1.76 ± 0.27	-1.99 ± 0.17	-1.96 ± 0.54	-2.12 ± 0.16
10% completeness	-1.55 ± 0.17	-1.63 ± 0.21	-1.66 ± 0.24	-1.64 ± 0.12
Final slope value	-2.00 ± 0.50	-1.97 ± 0.50	-2.28 ± 0.50	-2.06 ± 0.60

5 Star formation rate density and implications for the reionization

Based on the obtained results on the Luminosity Function, Chapter 5 focuses on luminosity density and the conversion of this parameter into star formation rate density by integrating the Luminosity Function with respect to luminosity. While the shape of the Luminosity Function at the bright part remains unaffected by the completeness threshold value, source selection and is consistent with the previous studies conducted in the blank fields, the faintest part is constrained by both these mentioned factors. For this reason, the result of the integration is not significantly influenced by the upper limitation, whereas the lower limitation is certainly an impacting factor.

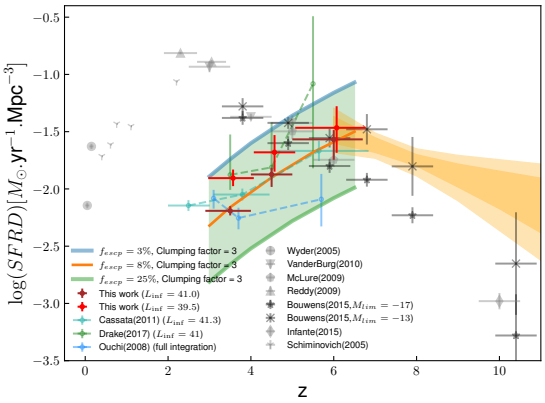

Figure 5.1: Evolution of star formation rate density with redshift. The red and brown-reddish crosses represent the results obtained when applying lower integration limits of log L [erg/s] = 39.5 and log L [erg/s] = 41.0, respectively. The blue, orange, and green solid lines indicate the critical values obtained with escape fraction values of 3%, 8% và 25%, combined with a typical clumping factor of 3.

I applied two lower limitation values: one is log L [erg/s] = 39.5 to cover all the data sample, and the other is log L [erg/s] = 41 to include only the most secure determinations of the LF. These results, when compared to the critical value for the star formation density (i.e., the amount required to reionize the Universe at a given redshift), suggest that galaxies selected by their Lyα emission could be responsible for reionization assuming a Lyα photon escape fraction of 8%, with a typical clumping factor of ~ 3 at redshift z ~ 6. In any case, they appear to play a substantial role in the reionization process.

6 Conclusions and perspective futures

The thesis presents a study of the contribution of star forming galaxies to the cosmic reionization via studying the Luminosity Function of Lyman alpha emitters in a redshift range of $2.9 \leq z \leq 6.7$ behind 17 lensing clusters observed by MUSE/VLT.
We selected 600 lensed LAEs that covered four orders of magnitude in magnification corrected Lyman alpha luminosity $39 \leq \log L[\mathrm{erg/s}] \leq 43$. In comparison with the previous data sample conducted by [7], the present data shows significant abundance (four times more) and contains more faint sources at $\log L \leq 41.0$ [erg/s]. The contribution of these sources to cosmic reionization has been measured by using the V_{max} method as the one presented in [7] with some improvements that have been introduced. The main results of the thesis have been listed and discussed as follows:

- The correlation between the magnification and cosmic co-moving volume of individual sources has been discussed. For the highly magnified sources, this correlation is shown by an exponential function when the magnification value of the sources was varied randomly within $2-\sigma$. While a linear function can be applied to the modest magnification sources.

- The evolution of the Luminosity Function with redshift has been investigated in four redshift intervals $2.9 \leq z \leq 4.0$, $4.0 \leq z \leq 5.0$, $5.0 \leq z \leq 6.7$ and $2.9 \leq z \leq 6.7$. The total co-moving volume of the survey is about $\sim 50000\ Mpc^3$, three times larger than the one found in [7]. However, this value is smaller than the ones used for data observed in the blank field. The explanation for this difference is a constraint of the magnification values caused by the lensing effect. The sources behind A2744 are still significant contributors to the total co-moving volume.

- The best fit values of the Schechter function in redshift interval $2.9 \leq z \leq 6.7$ are $\alpha = -2.06^{+0.07}_{-0.05}$, $\Phi*[10^{-4}\ \mathrm{Mpc}^3] = 7.41^{+2.70}_{-2.20}$, $\log L[\mathrm{erg/s}] = 42.85^{+0.10}_{-0.10}$.

- When $\log L[\mathrm{erg/s}] > 42$, our LF points are consistent with literature using data observed in blank fields and lensing fields.

- The contribution of the faint sources has been determined. Most of them are highly magnified sources. The slope values obtained from Schechter fitting and a linear fitting are consistent with the uncertainties. The slope values in four redshift intervals are in line with the literature, i.e., [15] and 20% higher than the ones obtained by [7]. This value also is in line with [16] in an interval redshift of $2.9 \leq z \leq 6.7$. When accounting for the effects of source selection, different completeness thresholds, the final slope values are -2.0 ± 0.50, -1.97 ± 0.50, -2.28 ± 0.50 and -2.06 ± 0.60 in redshift interval $2.9 \leq z \leq 4.0$, $4.0 \leq z \leq 5.0$, $5.0 \leq z \leq 6.7$ and $2.9 \leq z \leq 6.7$, respectively.

- The direct comparison to the results obtained by [7], the slope values of the Schechter function show evolution with redshift however, the uncertainty in each redshift interval is still large. We found a turnover in the shape of the Luminosity Function at the two highest redshift intervals, $4.0 \leq z \leq 5.0$ and $5.0 \leq z \leq 6.7$ when $\log L$ [erg/s] ≤ 41. This is explained

by the inefficiency of star formation in low-mass dark matter halos with masses below 10^{-9} Solar mass ([17, 18]).

- The results obtained from studying the evolution of the Luminosity Function with redshift have been used to estimate the contribution of star forming galaxies to the cosmic re-ionization.

- The contribution of LAEs is significant in maintaining the ionized state of Hydrogen atoms in the Universe. At redshift $z \sim 6$, its contribution is comparable to the LBGs.

- As mentioned above, uncertainties of measurements in the thesis are still large when estimating the contribution of Lyman alpha emitters to the cosmic re-ionization. Using data observed from different telescopes and different redshifts can help to improve the results obtained from the thesis.

Subsequently, I hope to continue this work on the Luminosity Function of Lyman alpha emitters using data collected behind 25 lens clusters belonging to the MUSE GTO program, or already available on the ESO archives. While doing the thesis, besides determining the redshifts of all the background galaxies from signatures of Lyα, I also did on other emission lines such as Balmer's series or OII-3727 at lower redshift. I also plan to work on JWST data and Euclid in a higher redshift range for Lyman alpha emitters. The excellent combination between JWST and MUSE also offers the possibility to analyze the production of ionizing photons with high efficiency.

THE NEW CONTRIBUTION OF THE THESIS

1- With 600 Lyman alpha line emission sources within a redshift range of $2.9 \leq z \leq 6.7$, this is the largest dataset of Lyman alpha emitting galaxies observed by gravitational lensing using the Multi Unit Spectroscopic Explorer (MUSE), installed on the Very Large Telescope (VLT) at the European Southern Observatory. The Lyman alpha Emitters (LAEs) in this sample were blindly detected and not subjected to any prior photometric selection, which typically favors strong continuum sources. Our sample covers four orders of magnitude in galaxy luminosity (10^{39} to 10^{44} erg s^{-1}) and efficiently probes the faint luminosity regime, down to 10^{40} erg s^{-1}. This sample sets a strong constraint on the luminosity function at the faint end as well as the evolution of the slope as a function of redshift. Hence, the data sample and the results presented in this thesis provide an important reference for further research in this field.

2- We have successfully developed a computational package that determines the volume of the Universe (Vmax) occupied by each galaxy detected in the survey for a large number of 17 gravitationally lensed galaxy clusters. This is the most important quantity in building the luminosity function to determine the number of galaxies in a given luminosity range per unit volume.

3- The steep slope of the Schechter luminosity function observed in previous studies persists in luminosity regions ten times fainter than those examined in previous blank field surveys. The steepening of the faint end slope with redshift, suggested by the earlier work is confirmed, but the uncertainties remain large.

4- Systematic uncertainties associated with computing the luminosity function in strong lensing fields are assessed, taking into account various factors including different gravitational lens models, flux measurements, completeness threshold cuts, and source selection effects.

5- Our results show that the star formation rate density of LAEs increases as a function of redshift. LAEs contribute significantly to the process of cosmic reionization.

LIST OF PUBLICATIONS

1. T. T. Thai, P. Tuan-Anh, R. Pello, I. Goovaerts, J. Richard, A. Claeyssens, G. Mahler , D. Lagattuta, G. de la Vieuville, E. Salvador-Solé, T. Garel, F. E. Bauer, A. Jeanneau , B. Clément, and J. Matthee. Probing the faint-end luminosity function of Lyman-alpha emitters at $3 \leq z \leq 7$ behind 17 MUSE lensing clusters. AA, 2023, 678, A139.

2. Ilias Goovaerts, Roser Pello, Tran Thi Thai, Pham Tuan-Anh, Johan Richard, Adélaïde Claeyssens, Emile Carinos, Geoffroy de la Vieuville, Jorryt Matthee. Evolution of the Lyman-α emitting fraction and UV properties of lensed star-forming galaxies between $2.9 \leq z \leq 6.7$. AA, 2023, 678, A174.

3. T. T. Thai, P. Tuan-Anh, R. Pello, I. Goovaerts. Studying the luminosity function of lyman alpha emitters selected behind 17 lensing clusters from multi-unit spectroscopic explorer (MUSE/VLT) observations. Proceeding in 16th OMEG conference.

Bibliography

[1] R. J. Bouwens et al. "UV Luminosity Functions at Redshifts z $\sim$ 4 to z $\sim$ 10: 10,000 Galaxies from HST Legacy Fields". In: 803.1, 34 (Apr. 2015), p. 34. DOI: 10.1088/0004-637X/803/1/34. arXiv: 1403.4295 [astro-ph.CO] (cit. on p. 2).

[2] Steven L. Finkelstein et al. "The Evolution of the Galaxy Rest-frame Ultraviolet Luminosity Function over the First Two Billion Years". In: 810.1, 71 (Sept. 2015), p. 71. DOI: 10.1088/0004-637X/810/1/71. arXiv: 1410.5439 [astro-ph.GA] (cit. on p. 2).

[3] Yechi Zhang et al. "First HETDEX Spectroscopic Determinations of Lyα and UV Luminosity Functions at z = 2-3: Bridging a Gap between Faint AGNs and Bright Galaxies". In: 922.2, 167 (Dec. 2021), p. 167. DOI: 10.3847/1538-4357/ac1e97. arXiv: 2105.11497 [astro-ph.GA] (cit. on p. 2).

[4] Masami Ouchi et al. In: 176.2 (June 2008), pp. 301–330. DOI: 10.1086/527673. arXiv: 0707.3161 [astro-ph] (cit. on p. 2).

[5] Akira Konno et al. "SILVERRUSH. IV. Lyα luminosity functions at z = 5.7 and 6.6 studied with $\sim$1300 Lyα emitters on the 14-21 deg^2 sky". In: 70, S16 (Jan. 2018), S16. DOI: 10.1093/pasj/psx131. arXiv: 1705.01222 [astro-ph.GA] (cit. on p. 2).

[6] G. Mahler et al. "Strong-lensing analysis of A2744 with MUSE and Hubble Frontier Fields images". In: 473.1 (Jan. 2018), pp. 663–692. DOI: 10.1093/mnras/stx1971. arXiv: 1702.06962 [astro-ph.GA] (cit. on p. 3).

[7] G. de la Vieuville et al. "Faint end of the z -7 luminosity function of Lyman-alpha emitters behind lensing clusters observed with MUSE". In: *A&A* 628 (2019), A3. DOI: 10.1051/0004-6361/201834471. URL: https://doi.org/10.1051/0004-6361/201834471 (cit. on pp. 4, 6, 9, 11, 12, 16, 20).

[8] Takatoshi Shibuya et al. In: *The Astrophysical Journal* 785.1 (Mar. 2014), p. 64. DOI: 10.1088/0004-637X/785/1/64. URL: https://dx.doi.org/10.1088/0004-637X/785/1/64 (cit. on p. 4).

[9] A. Claeyssens et al. "The Lensed Lyman-Alpha MUSE Arcs Sample (LLAMAS). I. Characterisation of extended Lyman-alpha halos and spatial offsets". In: 666, A78 (Oct. 2022), A78. DOI: 10.1051/0004-6361/202142320. arXiv: 2201.04674 [astro-ph.GA] (cit. on pp. 4, 6).

[10] Maarten Schmidt. "Space Distribution and Luminosity Functions of Quasi-Stellar Radio Sources". In: 151 (Feb. 1968), p. 393. DOI: 10.1086/149446 (cit. on p. 9).

[11] Hakim Atek et al. “The extreme faint end of the UV luminosity function at z 6 through gravitational telescopes: a comprehensive assessment of strong lensing uncertainties”. In: *Monthly Notices of the Royal Astronomical Society* 479.4 (July 2018), pp. 5184–5195. ISSN: 0035-8711. DOI: 10.1093/mnras/sty1820. eprint: https://academic.oup.com/mnras/article-pdf/479/4/5184/25207621/sty1820.pdf. URL: https://doi.org/10.1093/mnras/sty1820 (cit. on p. 13).

[12] R. J. Bouwens et al. “z 2–9 Galaxies Magnified by the Hubble Frontier Field Clusters. II. Luminosity Functions and Constraints on a Faint-end Turnover”. In: *The Astrophysical Journal* 940.1 (Nov. 2022), p. 55. DOI: 10.3847/1538-4357/ac86d1. URL: https://dx.doi.org/10.3847/1538-4357/ac86d1 (cit. on p. 13).

[13] T. Garel et al. In: *Monthly Notices of the Royal Astronomical Society* 504.2 (Apr. 2021), pp. 1902–1926. DOI: 10.1093/mnras/stab990. URL: https://doi.org/10.1093%2Fmnras%2Fstab990 (cit. on pp. 15, 16).

[14] Eduard Salvador-Solé et al. In: *The Astrophysical Journal* 936.2 (Sept. 2022), p. 178. DOI: 10.3847/1538-4357/ac874c. URL: https://doi.org/10.3847%5C%2F1538-4357%5C%2Fac874c (cit. on pp. 15, 16).

[15] Alyssa B. Drake et al. In: 471.1 (Oct. 2017), pp. 267–278. DOI: 10.1093/mnras/stx1515. arXiv: 1609.02920 [astro-ph.GA] (cit. on p. 20).

[16] Edmund Christian Herenz et al. In: 621, A107 (Jan. 2019), A107. DOI: 10.1051/0004-6361/201834164. arXiv: 1810.05037 [astro-ph.GA] (cit. on p. 20).

[17] Jason Jaacks et al. In: *The Astrophysical Journal* 766.2 (Mar. 2013), p. 94. DOI: 10.1088/0004-637X/766/2/94. URL: https://dx.doi.org/10.1088/0004-637X/766/2/94 (cit. on p. 21).

[18] Bin Yue et al. “On the faint-end of the high-z galaxy luminosity function”. In: *Monthly Notices of the Royal Astronomical Society* 463.2 (Aug. 2016), pp. 1968–1979. ISSN: 0035-8711. DOI: 10.1093/mnras/stw2145. eprint: https://academic.oup.com/mnras/article-pdf/463/2/1968/9686521/stw2145.pdf. URL: https://doi.org/10.1093/mnras/stw2145 (cit. on p. 21).